SOURCE-PLANE RECONSTRUCTION OF THE GIANT GRAVITATIONAL ARC IN A2667: A CANDIDATE WOLF–RAYET GALAXY AT z ~ 1

Shuo Cao, Giovanni Covone, Eric Jullo, Johan Richard, Luca Izzo, Zong-Hong Zhu

▶ **To cite this version:**

HAL Id: hal-01109685

https://hal.archives-ouvertes.fr/hal-01109685

Submitted on 26 Jan 2015

SOURCE-PLANE RECONSTRUCTION OF THE GIANT GRAVITATIONAL ARC IN A2667: A CANDIDATE WOLF–RAYET GALAXY AT $z \sim 1$

Shuo Cao[1,2], Giovanni Covone[2,3], Eric Jullo[4], Johan Richard[5], Luca Izzo[6,7], and Zong-Hong Zhu[1]

[1] Department of Astronomy, Beijing Normal University, 100875 Beijing, China; zhuzh@bnu.edu.cn
[2] Dipartimento di Scienze Fisiche, Università di Napoli "Federico II," Via Cinthia, I-80126 Napoli, Italy
[3] INFN Sez. di Napoli, Compl. Univ. Monte S. Angelo, Via Cinthia, I-80126 Napoli, Italy
[4] OAMP, Laboratoire d'Astrophysique de Marseille, UMR6110, Traverse du Siphon, F-13012 Marseille, France
[5] CRAL, Observatoire de Lyon, Universite Lyon 1, 9 Avenue Ch. Andre, F-69561 Saint Genis Laval Cedex, France
[6] Dip. di Fisica, Sapienza Universit'a di Roma, Piazzale Aldo Moro 5, I-00185 Rome, Italy
[7] ICRANet, Piazza della Repubblica 10, I-65122 Pescara, Italy

ABSTRACT

We present a new analysis of *Hubble Space Telescope, Spitzer Space Telescope,* and Very Large Telescope imaging and spectroscopic data of a bright lensed galaxy at $z = 1.0334$ in the lensing cluster A2667. Using this high-resolution imaging, we present an updated lens model that allows us to fully understand the lensing geometry and reconstruct the lensed galaxy in the source plane. This giant arc gives a unique opportunity to view the structure of a high-redshift disk galaxy. We find that the lensed galaxy of A2667 is a typical spiral galaxy with a morphology similar to the structure of its counterparts at higher redshift, $z \sim 2$. The surface brightness of the reconstructed source galaxy in the z_{850} band reveals the central surface brightness $I(0) = 20.28 \pm 0.22$ mag arcsec^{-2} and a characteristic radius $r_s = 2.01 \pm 0.16$ kpc at redshift $z \sim 1$. The morphological reconstruction in different bands shows obvious negative radial color gradients for this galaxy. Moreover, the redder central bulge tends to contain a metal-rich stellar population, rather than being heavily reddened by dust due to high and patchy obscuration. We analyze the VIMOS/integral field unit spectroscopic data and find that, in the given wavelength range ($\sim$1800–3200 Å), the combined arc spectrum of the source galaxy is characterized by a strong continuum emission with strong UV absorption lines (Fe II and Mg II) and shows the features of a typical starburst Wolf–Rayet galaxy, NGC 5253. More specifically, we have measured the equivalent widths of Fe II and Mg II lines in the A2667 spectrum, and obtained similar values for the same wavelength interval of the NGC 5253 spectrum. Marginal evidence for [C III] 1909 emission at the edge of the grism range further confirms our expectation.

Key words: galaxies: clusters: individual (A2667) – gravitational lensing: strong

1. INTRODUCTION

Considerable advances have been made over the last 15 yr to chart and investigate the properties and evolution of disk galaxies, which may provide insight into the galaxy formation process in a dark-matter-dominated universe. Moreover, it is well known that the galaxy stellar disks cannot only be thickened by interactions with low-mass halos (Benson et al. 2004), but also be entirely disrupted by the galaxies or by halos with galaxy masses (Koda et al. 2008). Therefore, the environments where these galaxies are located also play a significant role in the basic observational features of the disk galaxy population.

Hubble Space Telescope (*HST*) imaging and spectroscopy of high-redshift disk galaxies provide critical diagnostics of their formation and evolution (e.g., Law et al. 2009; Cassata et al. 2010). However, there are several observational challenges in pursuing the evolution history of disk galaxies beyond $z \simeq 1$. On one hand, observations of low surface brightness galaxies at $z \simeq 1$ are very challenging, thus limiting the size of the available data; on the other hand, at high redshift it becomes increasingly more difficult to resolve the spatial structure within galaxies, greatly restraining the possibility of understanding the exact position where processes (like star formation) occur. Consequently, gravitationally lensing galaxy clusters provide a unique and detailed view of the high-redshift universe, allowing us to probe the faint population of distant, background galaxies. This technique, often referred to as "gravitational telescope,"

was first proposed by Zwicky (1937) and has developed into an important astrophysical tool since the advent of the *HST*, since lensed galaxies are magnified by typically 1–3 mag and spatial sizes are correspondingly stretched (Kneib et al. 2005; Bradley et al. 2008; Zheng et al. 2009).

A magnificent gravitational lensing example is provided by the galaxy cluster A370 at $z = 0.375$ (Soucail et al. 1987; Lynds & Petrosian 1989), showing a giant gravitational arc ($z = 0.725$; Richard et al. 2010) that has been extensively analyzed with the multiband *HST*/ACS images. The galaxy cluster has a large Einstein radius, $\theta_E = 39'' \pm 2''$, for a source redshift at $z = 2$, and strong magnification in the central region makes A370 one of the best clusters to search for high-redshift galaxies. The first metallicity gradient measurement for a face-on spiral galaxy at $z \sim 1.5$ was also discussed by Yuan et al. (2011), through the analysis of the arc produced by the massive galaxy cluster MACS J1149.5+2223 at $z = 0.544$. More recently, Sharon et al. (2012) successfully reconstructed the source plane of a bright lensed galaxy at $z = 1.7$ magnified by the lensing cluster RCS2 032727−132623, using new high-resolution imaging from *HST*/Wide Field Camera 3. A similar rare case was discovered in VIMOS integral field unit (IFU) spectroscopic observations of the X-ray luminous cluster A2667 ($z = 0.233$).

The galaxy cluster A2667 is another remarkable example of "gravitational telescope." It is among the most luminous galaxy clusters in the X-ray sky (Ebeling et al. 1996), with a regular

X-ray morphology (Newman et al. 2013; Weißmann et al. 2013) and a cool core (Covone et al. 2006a). A redshift survey in the central acrmin square reveals a unimodal velocity distribution of the member galaxies (Covone et al. 2006b). A2667 shows a remarkable giant gravitational arc (Sand et al. 2005) originating from a blue star-forming galaxy at $z = 1.034 \pm 0.005$ (Covone et al. 2006b), and a system of lensed sources at high redshift (Laporte et al. 2011, 2012). Covone et al. (2006b) performed a wide-field integral field spectroscopy survey of the central arcmin square, using the VIMOS IFU, and built a strong lensing model using *HST*/WFPC2 data. Yuan et al. (2012) used this lensing model to derive the source-plane morphology from the archive WFPC2 data. They analyzed Keck II/OSIRIS spatially resolved near-infrared (NIR) spectra and found that the higher [N II]/Hα ratio in the outer region might be contaminated by a significant fraction of shock excitation due to galactic outflows.

In this paper, we extend the previous analysis on the magnified source of the giant arc in A2667, based on *HST*/ACS z_{850} imaging data and a set of complementary imaging and spectroscopic data. We improve the previous lensing model, produce a new inversion of the source galaxy, and study in detail the color gradient in this $\sim$1 system. The paper is organized as follows. In Section 2, we present the observational data used in this work. The lensing analysis, including a new lensing model, is presented in Section 3. Section 4 shows the physical conditions and main properties of the reconstructed source galaxy. A discussion and conclusions appear in Section 5. We assume a flat cosmology with $\Omega_\Lambda = 0.7$, $\Omega_m = 0.3$, and $H_0 = 70$ km s^{-1} Mpc^{-1}. All magnitudes refer to those in the AB system.

2. OBSERVATIONS

In this section, we will present the imaging and spectroscopic data used in the analysis of A2667. We use the imaging data from the *HST*, taken with the Advanced Camera for Surveys (ACS; Program 10504, PI: R. Ellis; filter *F850LP*), WFPC2 (Program 8882, PI: Allen; filters *F450W*, *F606W*, and *F814W*), and Near-Infrared Camera and Multi-Object Spectrometer (NICMOS; Program 10504, PI: R. Ellis) and ground-based data from ISAAC at the Very Large Telescope (VLT; Program 71.A-0428, PI: J.-P. Kneib) through the *F110W* and *F160W* filters. *HST* high-resolution images are essential to building an accurate model of the gravitational lens, while the large multi-wavelength coverage allows us to constrain the properties, for example, the color gradient of the lensed source in different bands.

The *HST*/WFPC2 observations were obtained on 2001 October 10–11, for a total of 12,000/5000/5000 s in the *F450W*/*F606W*/*F814W* bands, respectively. The final data have a depth of $\simeq$25 mag. Compared to the WFPC2 observations, the *HST*/ACS data in the *F850LP* band cover a square field of about 18 acrmin^2, are deeper, and have higher resolution. The final data were obtained on 2006 July 21 for a total of 8765 s, and have a pixel scale of 0$\farcs$05 with a depth of $z_{850} \simeq 28$. The NIR imaging data are observed from NICMOS in broad-, medium-, and narrowband filters, broadband imaging polarimetry, coronagraphic imaging, and slitless grism spectroscopy. The NICMOS observations were obtained on 2006 August 6, for a total of 4608/7104 s in the *F110W*/*F160W* bands with a depth of $\simeq$27 mag. Moreover, the mid-infrared data for A2667, which were obtained with *Spitzer*/IRAC (Program 83, PI: G. Rieke; Program 60034, PI: E. Egami), were also used for the multiband photometric measurements presented in Section 4. The final *Spitzer*/IRAC data were acquired using four broadband filters in the IR channel, and centered at 3.6, 4.5, 5.8, and 8.0 μm.

The central region of the galaxy cluster was observed with the VIMOS IFU (Covone et al. 2006b; Grin et al. 2007) mounted on VLT Melipal, with a field of view of $54'' \times 54''$, fiber size 0$\farcs$66, and the low-resolution red grism ($R \sim 250$), covering from about 3900–5300 Å. Covone et al. (2006b) extracted 22 galaxy spectra and the spatially resolved spectra of 3 lensed images of the gravitational arc.

3. STRONG LENSING MASS MODEL

We used the publicly available software LENSTOOL[8] (Jullo et al. 2007) to compute the best-fit lens model. LENSTOOL makes use of a Monte Carlo Markov Chain (MCMC) optimization method.

The source galaxy is multiply imaged into three images (A1, A2, and A3; see Figure 1)[9]: two of them (A1 and A2) are merged, forming the giant gravitational arc located 14$''$ northeast of the brightest cluster galaxy (BCG), while A3 constitutes an isolated system. The clear mirror symmetry along the giant arc provides additional constraints on the location of the critical line at the arc redshift. *HST*/ACS data allow us to identify unambiguously multiply imaged subregions within the three images (Figures 1(b) and (c)).

We use the *HST*/ACS to build a new lensing model of matter distribution in the cluster core. The positions of the images are the main input observational data to constrain the lens model parameters. We determine the position of the brightest peak for each multiply lensed feature in the arc, assuming a position error of 0$\farcs$05 (the spatial resolution of the *HST*/ACS data per pixel); see also Faure et al. (2011), Cao et al. (2013), and Collett & Auger (2014).

To model the mass distribution, we include both a cluster mass-scale component (representing the contribution of dark matter and the baryonic gas halo) and cluster galaxy mass components (Kneib et al. 1996; Smith et al. 2005). Bright cluster galaxies within the central $\sim$1 arcmin^2 belonging to the galaxy cluster are selected according to their redshift, while massive galaxies along the line of sight are also included, with their lensing properties rescaled at the cluster redshift. All the model components (including the large-scale cluster halo, the BCG, and individual galaxies) are parameterized using a pseudo-isothermal mass distribution model (PIEMD; Kassiola & Kovner 1993), which is determined by its position x, y; ellipticity $e = (a^2 - b^2)/(a^2 + b^2)$, where a and b are the semimajor and semiminor axes, position angle θ, velocity dispersion σ_0, core radius $r_{\rm core}$, and truncation radius $r_{\rm cut}$.

The best-fit lensing mass model is found by fitting the position, ellipticity, orientation, and mass parameters (velocity dispersion, core, and truncation radii) of the cluster-scale component. The center of the BCG (x and y) is fixed at the observed values in the ACS image, while the other parameters (the ellipticity, orientation, and mass parameters) are set free. Other galaxies are individually chosen to have the same position, ellipticity, and orientation as their corresponding z_{850} band image. The effect of the mass distributions of the most massive member galaxies Gal2–Gal4 are taken into consideration with only one free parameter, the central velocity dispersion σ_0. By assuming a Faber & Jackson (1976) relation and a global mass-to-light ratio (M/L), the masses of the other galaxies are scaled according to

---

8 http://projets.lam.fr/projects/lenstool/wiki
9 Hereafter, we use the same notation for the lensed images as in Covone et al. (2006b).
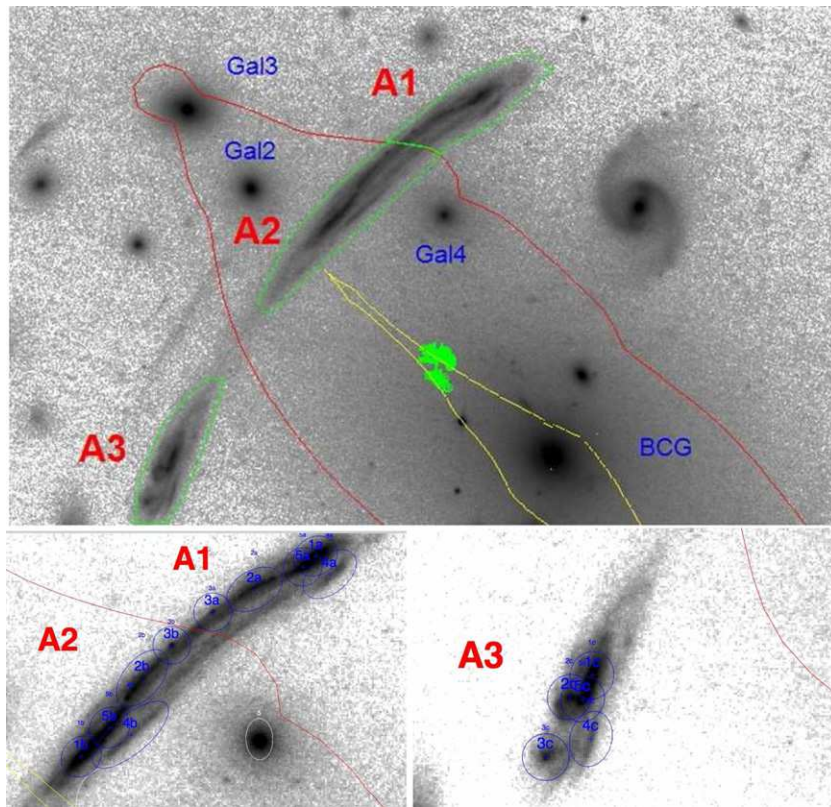
Figure 1. *HST*/ACS image of A2667 in the z_{850} band. Top panel: constraint results with the image-plane critical curves overplotted in red and the source-plane caustic in yellow. The favored source positions are denoted by green ellipses. The giant arc is indicated as A1–A3 within three green polygonal apertures. North is to the top and east to the left. Bottom panels: location of matched regions identified with colored ellipses in each part of the giant arc.

Table 1
Best-fit Lens Model Parameters

Halo (PIEMD)	R.A. ($''$)	Decl. ($''$)	e	θ (deg)	r_{core} ($''$)	r_{cut} ($''$)	σ_0 (km s^{-1})
Cluster	-0.15 ± 1.54	-0.54 ± 1.47	0.58 ± 0.15	-42.43 ± 3.43	15.32 ± 4.97	228.30 ± 140.08	887 ± 116
BCG	0	0	0.21 ± 0.20	-43.52 ± 16.89	0.85 ± 0.28	44.30 ± 13.48	169 ± 43
Gal2	-12.71	11.34	0.25	-41.40	...	...	65 ± 20
Gal3	-15.42	14.66	0.17	-9.40	...	...	123 ± 28
Gal4	-4.53	10.21	0.41	-88.40	...	...	103 ± 25
L* galaxy	...	...	...	...	...	22.03 ± 6.83	111 ± 28

Note. All coordinates are measured relative to the center of the BCG at [R.A., decl.] = [357.914250, −26.084105].

their *K*-band luminosity estimated using a typical E/S0 spectral energy distribution (SED; Covone et al. 2006b). Therefore, the truncation radius and the velocity dispersion are the two independent parameters of the ensemble of cluster galaxies. The best-fit values of the model parameters and their uncertainties are summarized in Table 1. The mean source-plane rms is $\simeq 0''.10$. Considering the ratio of the sizes between the image-plane and the source-plane reconstruction, we obtain the total flux magnification for the giant arc, $\mu = 14.0 \pm 2.0$, consistent with the result of Yuan et al. (2012).

4. PROPERTIES OF THE SOURCE GALAXY

4.1. Source Reconstruction

The gravitational lensing model enables us to derive the source-plane properties independently through each of the three images A1–A3. The source-plane reconstruction is performed by using the task `cleanlens` in LENSTOOL, computing the corresponding position in the source plane for each point of the image plane through the best-fit lens model. There are two related subsampling parameters in our analysis, *echant* and *s-echant*. With *echant* = 2, each pixel in the CCD frame will be cut into four smaller pixels during the calculation of the source frame. The *s-echant* parameter plays the same role when subsampling the frame in the source plane. In our analysis, *echant* and *s-echant* are both fixed at 2.

We extract the giant arc within three polygonal apertures constructed to enclose the whole lensed system (see Figure 1). Figure 2 shows the three independent reconstructions of the source from the three different lensed images, separately, as well as the result obtained by considering the three images simultaneously. The overall agreement between the three source reconstructions from individual images validates the best-fit model.

In order to take into account the uncertainties of the best-fit lens model parameters, we produce 600 source-plane images
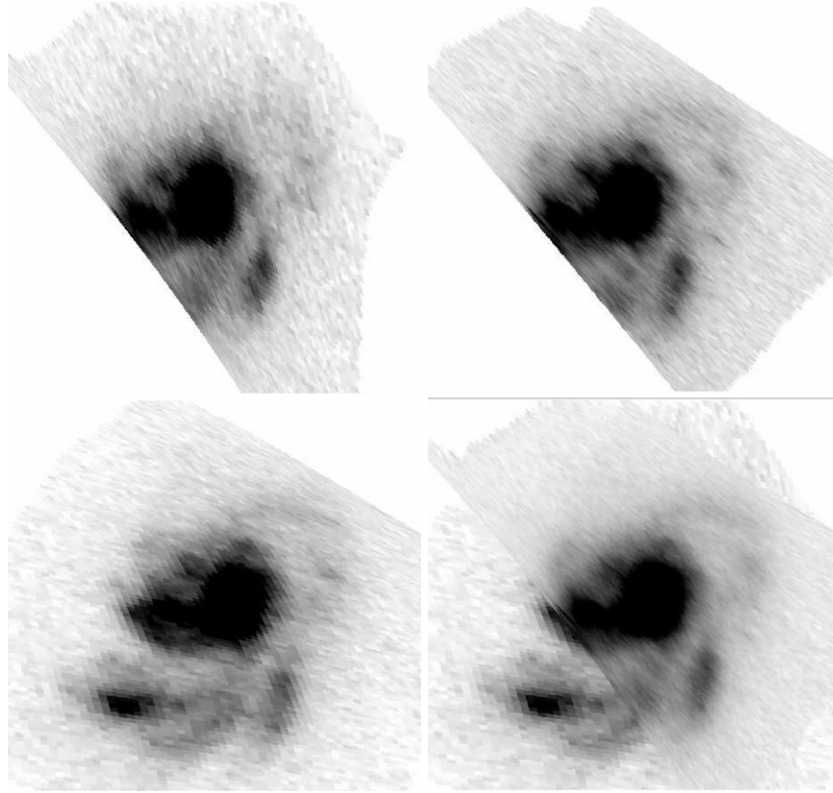
Figure 2. Source reconstruction from each of the magnified images of the giant arc and their rendition into one frame with the best-fit lens model.
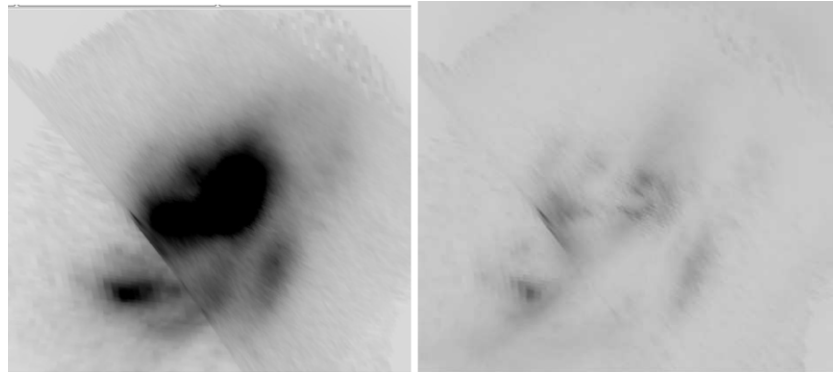

Figure 3. Source reconstruction results from MCMC simulations. Left: source reconstruction with mean values of the lens model parameters. Right: errors on the source reconstruction given the uncertainties on the lens model parameters. Note that model-based systematic uncertainties and measurement noise are both included for the reconstructed source-plane image.

through an MCMC simulation, which are then combined to obtain information on the uncertainties on the reconstructed source. The simulation results are shown in Figure 3. The scatter in the pixel values tells us about the impact of the lens model on our reconstruction. We find that the largest systematic errors on the source reconstruction come from the two clumps on the southeast (about 20%) and the faint spiral arms (about 15%). As for the central bulge of the galaxy, the effect of the reconstruction errors is relatively small (about 10%).

On the basis of the reconstructed source from WFPC2 data of image A3, Yuan et al. (2012) could not resolve between a merging system and a disturbed disk galaxy. In our reconstruction from the three images, the source galaxy appears to be an asymmetric disk galaxy with a bright central bulge and tightly wrapped spiral arms. This picture is also confirmed by the regular and smooth exponential profile shown in the disk (see Section 4.2) and by the small velocity gradient across the

disk found by Yuan et al. (2012) based on the observations of the Hα emission line. Hence, the source is approximately a face-on rotating disk or a non-rotating system.

4.2. Multiband Photometry

A detailed photometric analysis in different wavebands is required to derive the color profile of the disk galaxy. Therefore, we used the fiducial best-fit lensing model based on the *HST*/ACS z_{850} image (see Table 1) to reconstruct the intrinsic source morphology in other bands and measure the luminosity profiles.

Figure 4 shows the surface brightness $I(R)$ (in units of mag arcsec^{-2}) of the reconstructed source galaxy from the z_{850} band image. Surface brightness is measured in elliptical regions, in order to take into account projection effects; by assuming intrinsic circular isophotes, we find an inclination angle (along the line of sight) $\theta = 40° \pm 5°$. In the stellar disk, when averaged over features like spiral arms, the surface brightness
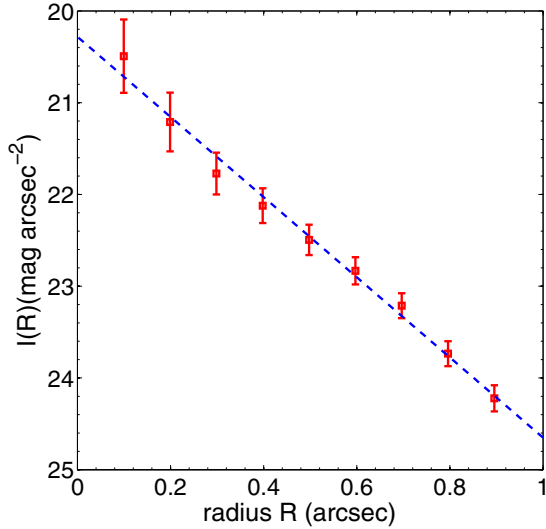
Figure 4. Surface brightness of the source galaxy in the z_{850} band. The dashed line is an exponential with $r_s = 2.01$ kpc ($h_R = 0.''25$). Surface brightness is given in units of mag arcsec^{-2}, the flux coming from each square arcsecond of the galaxy, expressed as an apparent magnitude.

approximately follows an exponential profile. When expressed in units of mag arcsec^{-2}, this reads

$$I(R) = I(0) + 1.086(R/h_R). \qquad (1)$$

At the center of the source galaxy, the z_{850} band surface brightness is $I(0) = 20.28 \pm 0.22$ mag arcsec^{-2}. Figure 4 shows the fit to the source z_{850} band surface brightness: the scale length is $h_R = 0.''25 \pm 0.''02$, corresponding to a linear radius $r_s = 2.01 \pm 0.16$ kpc at the source redshift. The apparent magnitude within r_s is $m_s = 23.6 \pm 0.6$. After correcting for the flux magnification, the intrinsic luminosity at the galaxy redshift is $L_* = 2.70^{+0.13}_{-0.08} \times 10^9 L_{\odot}$.

Yuan et al. (2012) measured the stellar mass of the source galaxy by fitting the SED. By assuming an extinction value $E(B - V) = 0.60$ and a star formation rate SFR$_{\rm SED} = 50 \pm 35\ M_{\odot}$ yr^{-1}, they estimated the stellar mass to be $\log M_* = 10.28 \pm 0.31$.

We can compare the source of the giant arc in A2667 with the large sample of disk galaxies at high-z observed by Miller et al. (2011). Based on spectra from DEIMOS on the Keck II Telescope, Miller et al. (2011) measured the evolving scaling relation of three types of disk-like galaxies in the redshift range $0.2 < z < 1.3$. Disk-like galaxies with extended line emission across the two-dimensional spectrum (like the A2667 giant arc source) have larger mean scale radii ($r_s = 2.68 \pm 0.09$ kpc) with respect to the compact ($r_s = 2.09 \pm 0.13$ kpc) and passive ($r_s = 2.24 \pm 0.16$ kpc) galaxy samples. Our system also has a stellar maximum very close to the average stellar mass of the disk-like galaxies in Miller et al. (2011), $\log M_* = 10.11 \pm 0.05$. Therefore, the giant arc source appears to be a typical disk galaxy at ~ 1. Note that the passive disk galaxies constitute the upper end of the total stellar mass with $\log M_* = 10.69 \pm 0.09$, while the typical values are $\log M_* = 10.21 \pm 0.10$ for the compact.

It is well known that the radial color gradient of a spiral galaxy provides a unique test of the star formation rate (SFR) along the disk and thus the disk formation and evolution. Multiband photometry of the reconstructed source in six different bands is presented in Figure 5. The lensed galaxy exhibits a negative gradient (i.e., the color is gradually bluer outward), as observed for most of the spiral galaxies (Moth & Elston 2002; MacArthur et al. 2004; Taylor et al. 2005). Moreover, the color profile becomes shallower with increasing radius and the color of this source galaxy is redder in the central bulge, which could be explained by either a standard bulge/disk structure with the center of this galaxy dominated by an old stellar population (Yuan et al. 2012), or by a merging/disturbed system that happens to have more attenuation by dust toward the center of the galaxy.

The above two possible causes can helpfully explain both the color gradient and the reddened central bulge of the target galaxy. Regarding the stellar population, it is broadly accepted that for galactic disks, the SFR) is proportional to the surface mass density (Bell & de Jong 2000; Kauffmann et al. 2003), but inversely proportional to the radius (Kennicutt et al. 1998; Boissier & Prantzos 1999). Therefore, the inner regions of spiral galaxies may possibly evolve faster than the outer regions, which leads directly to older metal-rich stellar populations in the center (Prantzos & Boissier 2000). As for the dust, many previous
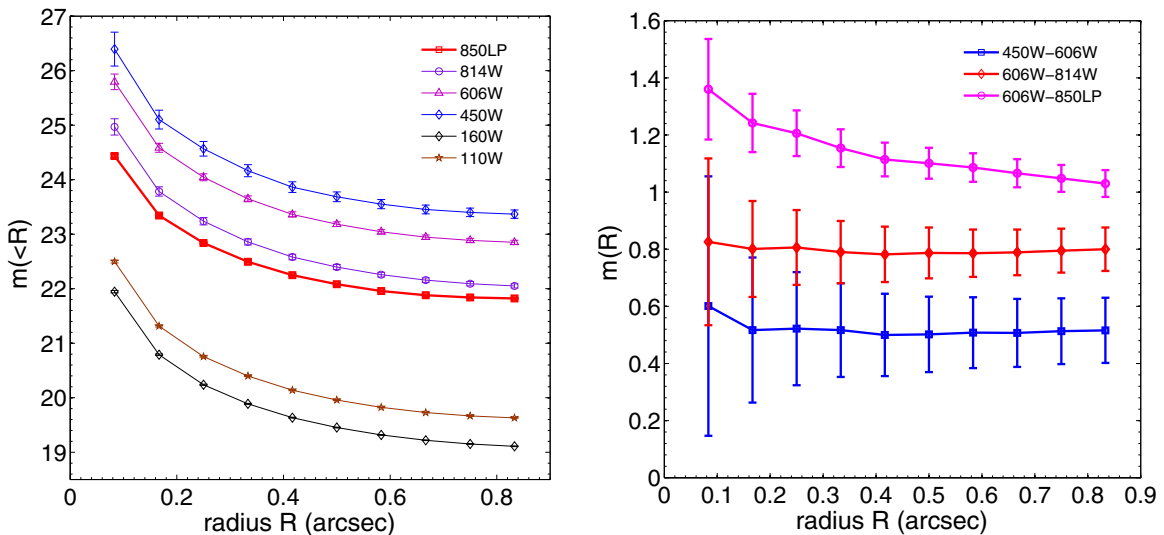

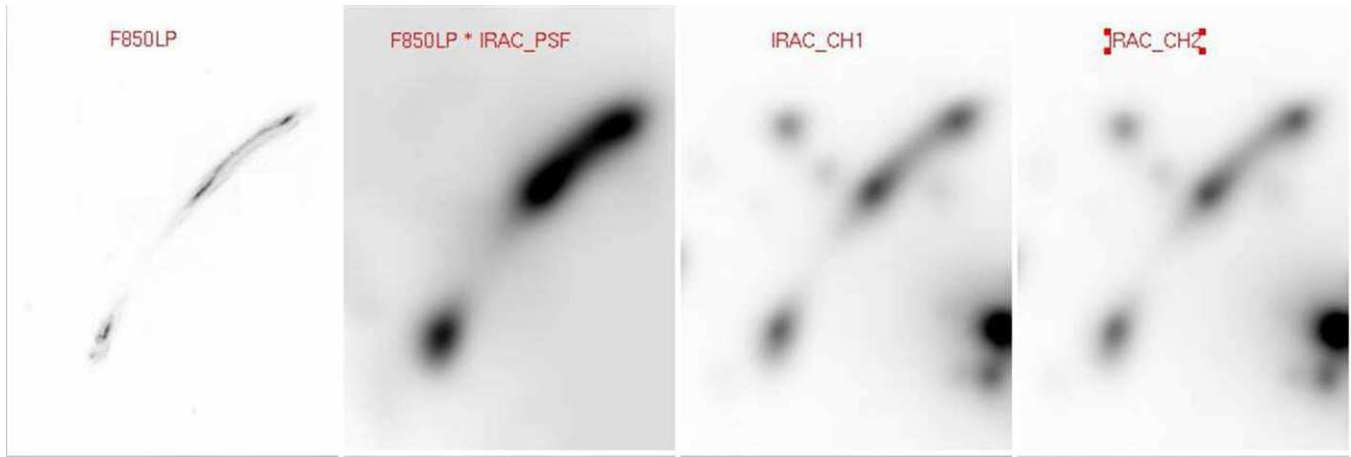**Figure 5.** Apparent magnitudes and color profiles of the source galaxy at different optical and NIR bands.

Figure 6. Shown is the process used to derive the colors $z_{850} - \mathrm{mag}_{3.6}$ and $z_{850} - \mathrm{mag}_{4.5}$ in different regions of the gravitational arc. From the left, the panels show the image of the arc in the *HST*/ACS, the *HST*/ACS data convolved with the *Spitzer*/IRAC PSF, and the arc observed with *Spitzer*/IRAC at 3.8 and 4.5 μm.

works also showed that its distribution along the disk of spiral galaxies might be proportional to the stellar mass density profile (Regan et al. 2006), which gives birth to an inner galactic region containing more dust and also naturally generates a negative color gradient.

We have measured the color gradient within a half-light radius R_{50} and obtained corresponding values of $B_{450} - V_{606} = 0.55$ and $V_{606} - I_{814} = 0.80$. To make a quantitative comparison, we compare with previous measurements of the color difference in galaxies observed in the GOODS-South Field (Welikala & Kneib 2012), which investigated the galactic radial variation of colors evolving with redshift. For a stacked bright sample like our case, the color differences are $0.6 < \delta(B - R) < 0.8$ for galaxies within the redshift ranges $0.79 < z < 0.95$ and $0.25 < \delta(B - R) < 0.5$ for high-redshift galaxies at $1.15 < z < 1.35$. Concerning the color gradient $\delta(R - I)$ within R_{50}, the corresponding values change to $0.8 < \delta(R - I) < 1.0$ for low-redshift galaxies ($0.5 < z < 1.0$) and $0.5 < \delta(R - I) < 0.7$ for high-redshift galaxies ($1.0 < z < 1.5$; Welikala & Kneib 2012). In our analysis, the calculated color gradients of the lensed galaxy of A2667, a spiral galaxy at $z \sim 1$, are in good quantitative agreement with the previous results above.

In order to determine the nature of the reddened galactic center, first, we make measurements of the apparent magnitude of the galaxy center within $0''.17$ (which corresponds to 1.34 kpc). As can be seen in Figure 5, the center of this galaxy is much redder ($B_{450} - V_{606} = 0.50$). Second, the colors $z_{850} - \mathrm{mag}_{3.6}$ and $z_{850} - \mathrm{mag}_{4.5}$ are also measured in the image plane. In order to perform photometric measurements on the *Spitzer*/IRAC data, we convolve the z_{850} *HST* image with the IRAC point-spread function (PSF) and subtract it, after rescaling, from the IRAC images (see Figure 6). As expected, the colors of the arc are quite different between the center of the spiral and the spiral arms. We find that in the bulge, $z_{850} - \mathrm{mag}_{3.6} = 0.23$ and $z_{850} - \mathrm{mag}_{4.5} = 0.03$. In the spiral arms, the color is much bluer: $z_{850} - \mathrm{mag}_{3.6} = -0.36$ and $z_{850} - \mathrm{mag}_{4.5} = -0.72$. The uncertainty on these colors is ~ 0.1 mag, as evaluated from the amount of residuals in the respective regions.

The theory of dust attenuation has been reviewed many times in different papers (MacArthur et al. 2004; Taylor et al. 2005). However, we lack theories with dust attenuation only to explain the fact that the center of this galaxy is too much brighter in the R band than the B band. From an observational point

of view, galaxies with high surface mass density always have more dust and generate steeper color gradients (Regan et al. 2006; Liu et al. 2009), i.e., the more luminous galaxies have steeper scaled color gradients, which is inconsistent with our observations. Consequently, dust attenuation only plays a minor role in regulating the color gradients of spiral galaxies, or at least could not be the only role in the origin of reddened galactic center (MacArthur et al. 2004; Taylor et al. 2005).

Thus, we can reach a careful conclusion that the central bulge of the lensed galaxy of A2667 tends to be heavily dominated by an old stellar population; meanwhile, the other two blue clumps on the south are very likely to be active star-forming regions and responsible for the starbursts of this blue star-forming galaxy (Yuan et al. 2012). Further constraints and discussion on the spectroscopic type of this star-forming galaxy are given in Section 4.3.

4.3. VIMOUS/IFU Spectroscopy

We discuss here the VIMOUS/IFU spectroscopic data collected by Covone et al. (2006b) in the given wavelength range (~ 1800–3200 Å). Figure 7 shows the combined spectrum as a blue line from the three images of the giant gravitational arc (i.e., summing the signal from all three images of the arc). The source shows the characteristic spectrum of a blue star-forming galaxy, with a strong UV continuum emission and evident spectral features due to low-ionization absorption lines (in particular, the strongest in our spectra are the [C III] 1909 line, the Fe II 2370/2600 lines, and the Mg II/2800 line).

We have compared the spectrum of the arc on A2667 with some galaxy templates, focusing particularly on starburst galaxies. Following the work of Leitherer et al. (2011), we have first compared the spectrum of the arc on A2667 with two templates of high- (orange spectrum) and low-metallicity (green spectrum) starbursting galaxies in Figure 7. The high-z spectrum is characterized by almost an absence of the [C III] 1909 line and more pronounced interstellar lines of Fe II, Mn II, and Mg II, while in the low-z spectrum the [C III] nebular line is very pronounced, but there is a lower intensity of the interstellar lines. In the spectrum of A2667, these absorption lines are all present, including the Mg I 2853 line. The resolution of the spectrum does not allow us to split the single Fe II–Mn II line and the Mg II doublet at 2796–2803 Å.
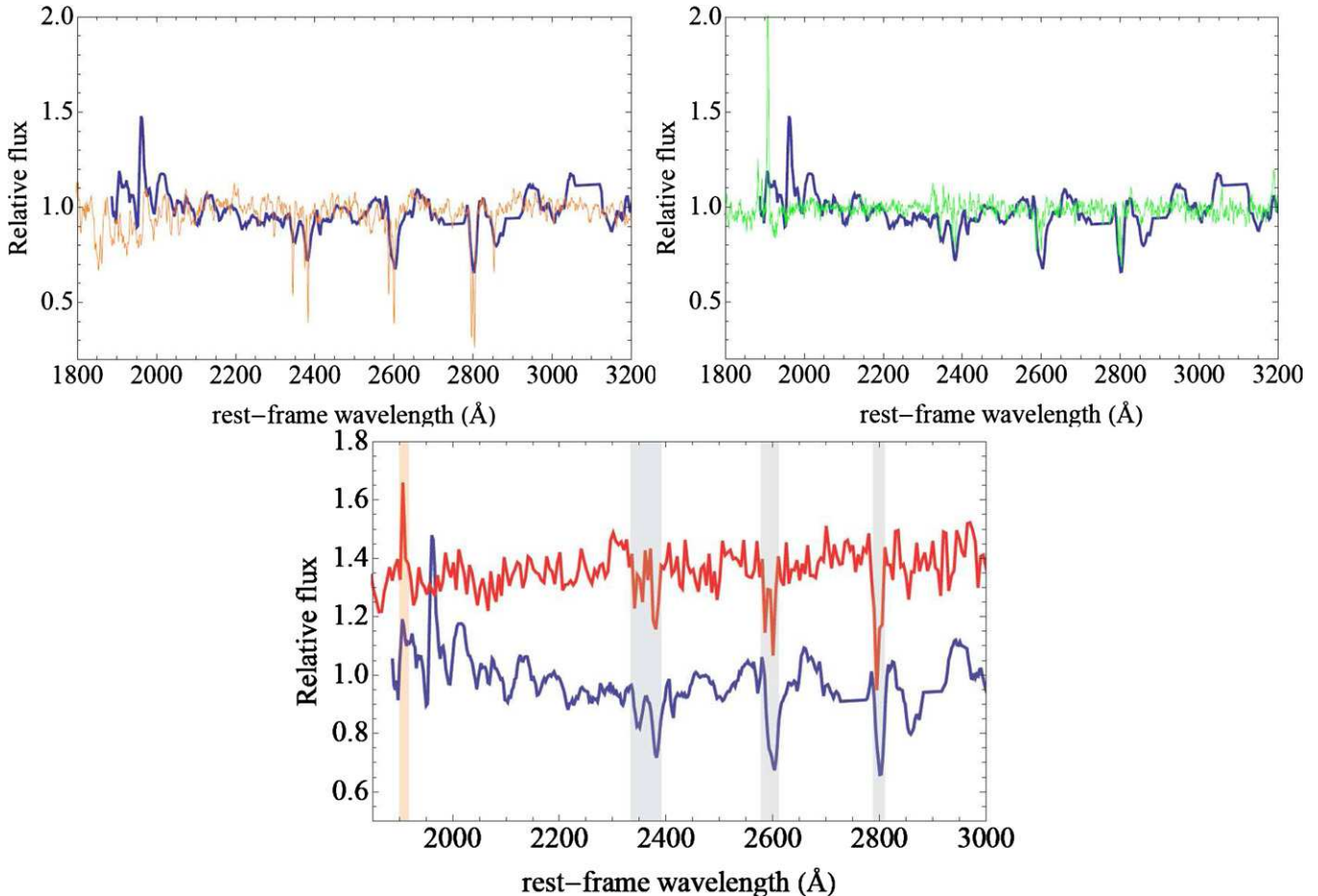
Figure 7. Arc spectrum of A2667 (blue spectrum) compared with two templates of high- (orange spectrum) and low-metallicity (green spectrum) starburst galaxies, as well as the UV spectrum of the local Wolf–Rayet galaxy NGC 5253 (red spectrum). The prominent features (e.g., the [C III] emission and some of the strong wind absorption features) that motivate the classification as a Wolf–Rayet galaxy spectrum are also identified. The gray shaded lines denote the EWs of Fe II and Mg II in the A2667 spectrum considering the same wavelength interval of the NGC 5253 spectrum, while the orange shaded line marks the presence of the [C III] line.

The presence of the [C III] line suggests a further spectra comparison with the starbursting Wolf–Rayet (WR) galaxy NGC 5253 from the database complied by Storchi-Bergmann et al. (2004, 2005). WR galaxies are a subset of blue emission-line galaxies showing the signature of large numbers of WR stars in their spectra (Vacca & Conti 1992). WR galaxies are thought to be undergoing current or very recent star formation, with a large population of massive stars in the age range $1 \sim 10 \times 10^6$ yr. NGC 5253 is a blue compact WR galaxy at a distance of 3.6 ± 0.2 Mpc (Sakai et al. 2004), showing an intense burst of star formation in the central region. With the measurements of the equivalent widths (EWs) of blended interstellar lines for NGC 5253 (Leitherer et al. 2011), we have measured the EWs in the arc on the A2667 spectrum, considering the same wavelength interval as with the NGC 5253 spectrum (gray shaded lines in Figure 7).

We obtain EW (Fe II 2370) = 5.42 ± 0.58, EW (Fe II 2600) = 6.77 ± 1.32, and EW (Mg II 2800) = 5.66 ± 1.26, similar to the values obtained for the NGC 5253 spectrum: EW (Fe II 2370) = 5.40 ± 0.82, EW (Fe II 2600) = 4.56 ± 0.51, and EW (Mg II 2800) = 5.27 ± 0.35. We then first infer a quite low metallicity (log[O/H] $\leqslant 8.5$) for the lensed galaxy A2667. In Figure 7, the presence of the [C III] line in the spectrum of NGC 5253 is also shown with the one in the arc on the A2667 spectrum (orange shaded line). The low-significance [C III] line in the spectra is

likely a product of the low-resolution VIMOS spectra, which makes it difficult to identify lines with relatively small EWs (Bayliss et al. 2013).

Meanwhile, we remark that the physical origin of the [C III] emission is not entirely certain, as it should in general be offset in velocity from absorption features that result from the large gas outflows that WR stars create. To fully understand the classification of the lensed galaxy, a higher-resolution spectrum is required to measure the velocity offsets between the [C III] emission and the Fe II and Mg II absorption lines.

5. DISCUSSION AND CONCLUSIONS

We used *HST*/ACS z_{850} imaging data to construct an improved lens model for the lensing cluster A2667. Using the new lens model, we reconstructed the de-lensed image of the source galaxy at $z \sim 1$. The source resembles a normal disk galaxy with a bright, large central bulge, and tightly wrapped spiral arms. Multiband imaging data allowed us to identify features of the lensed source galaxy in different bands. We summarize our main findings here.

1. The surface brightness $I(R)$ (Figure 4) of the reconstructed source galaxy from the CCD image in the z_{850} band reveals the central surface brightness

$I(0) = 20.28 \pm 0.22$ mag arcsec^{-2} and the exponential slope with scale length $h_R = 0''.25 \pm 0''.02$ (a characteristic radius $r_s = 2.01 \pm 0.16$ kpc at redshift $z = 1.0334$). The smooth exponential profile supports the hypothesis of a mildly disturbed, almost face-on, disk versus a merging system, consistent with the velocity structure observed by Yuan et al. (2012).

2. After correcting for the flux magnification, the intrinsic luminosity of this spiral galaxy is $L_* = 2.70^{+0.13}_{-0.08} \times 10^9 L_\odot$, with the corresponding stellar mass $\log M_* = 10.28 \pm 0.31$. These values are close to those of disk galaxies with extended emission lines observed at $z > 1$ (Miller et al. 2011).

3. There are negative radial color gradients along the disk (i.e., the color is gradually bluer outward). The color profile becomes shallower with increasing radius, which provides unique star-forming information along the disk and thus the history of disk formation and evolution. Moreover, we find that the central region of the galaxy tends to contain more metal-rich stellar populations, rather than being heavily reddened by dust due to high and patchy obscuration.

4. We further analyze the archive VIMOUS/IFU spectroscopic data (Covone et al. 2006b) and find that the spectra of the source galaxy with the giant gravitational arc is characterized by a strong continuum emission with strong UV absorption lines (Fe II and Mg II). Moreover, in the given wavelength range ($\sim$1800–3200 Å) of the combined arc spectrum, the lensed galaxy of A2667 shows some typical features of a typical starburst WR galaxy (NGC 5253) with strong signatures from large numbers of WR stars (Figure 7). More specifically, we have measured the EWs in the A2667 spectrum considering the same wavelength interval of the NGC 5253 spectrum, and obtained EW (Fe II 2370) = 5.42 ± 0.58, EW (Fe II 2600) = 6.77 ± 1.32, and EW (Mg II 2800) = 5.66 ± 1.26, which are similar to the values for the NGC 5253 spectrum. Marginal evidence for [C III] 1909 emission at the edge of the grism range, as expected for a typical WR galaxy, further confirms our expectation. However, this conclusion still needs to be checked with a high-resolution spectrum covering a different wavelength range.

REFERENCES

Bayliss, M. B., Rigby, J. R., Sharon, K., et al. 2013, ApJ, 790, 144
Bell, E. F., & de Jong, R. S. 2000, MNRAS, 312, 497
Benson, A. J., Lacey, C. G., Frenk, C. S., Baugh, C. M., & Cole, S. 2004, MNRAS, 351, 1215
Boissier, S., & Prantzos, N. 1999, MNRAS, 307, 857
Bradley, L. D., Bouwens, R. J., Ford, H. C., et al. 2008, ApJ, 678, 647
Cao, S., Covone, G., Paolillo, M., & Zhu, Z.-H. 2013, RAA, 13, 15
Cassata, P., Giavalisco, M., Guo, Y., et al. 2010, ApJL, 714, L79
Collett, T. E., & Auger, M. W. 2014, MNRAS, 443, 969
Covone, G., Adami, C., Durret, F., et al. 2006a, A&A, 460, 381
Covone, G., Kneib, J.-P., Soucail, G., et al. 2006b, A&A, 456, 409
Ebeling, H., Voges, W., Bohringer, H., et al. 1996, MNRAS, 281, 799
Faber, S. M., & Jackson, R. E. 1976, ApJ, 204, 668
Faure, C., Anguita, T., Alloin, D., et al. 2011, A&A, 529, A72
Grin, D., Covone, G., Kneib, J.-P., et al. 2007, PhRvD, 75, 105018
Jullo, E., Kneib, J.-P., Limousin, M., et al. 2007, NJPh, 9, 447
Kassiola, A., & Kovner, I. 1993, ApJ, 417, 450
Kauffmann, G., Heckman, T. M., White, S. D. M., et al. 2003, MNRAS, 341, 54
Kennicutt, R. C. 1998, ApJ, 498, 541
Kneib, J.-P., Ellis, R. S., Santos, M. R., & Richard, J. 2004, ApJ, 607, 697
Kneib, J.-P., Ellis, R. S., Smail, I., Couch, W. J., & Sharples, R. M. 1996, ApJ, 471, 643
Koda, J., Milosavljevic, M., & Shapiro, P. R. 2009, ApJ, 696, 254
Laporte, N., Pelló, R., Hayes, M., et al. 2012, A&A, 542, L31
Laporte, N., Pelló, R., Schaerer, D., et al. 2011, A&A, 531, A74
Law, D. R., Steidel, C. C., Erb, D. K., et al. 2009, ApJ, 697, 2057
Leitherer, C., Tremonti, C. A., Heckman, T. M., & Calzetti, D. 2011, AJ, 141, 37
Liu, C.-Z., Shen, S.-Y., Shao, Z.-Y., et al. 2009, RAA, 9, 1119
Lynds, R., & Petrosian, V. 1989, ApJ, 336, 1
MacArthur, L. A., Courteau, S., Bell, E., & Holtzman, J. A. 2004, ApJS, 152, 175
Miller, S. H., Bundy, K., Sullivan, M., Ellis, R. S., & Treu, T. 2011, ApJ, 741, 115
Moth, P., & Elston, R. J. 2002, AJ, 124, 1886
Newman, A. B., Treu, T., Ellis, R. S., et al. 2013, ApJ, 765, 24
Prantzos, N., & Boissier, S. 2000, MNRAS, 313, 338
Regan, M. W., Thornley, M. D., Vogel, S. N., et al. 2006, ApJ, 652, 1112
Richard, J., Kneib, J.-P., Limousin, M., Edge, A., & Jullo, E. 2010, MNRAS, 402, L44
Sakai, S., Ferrarese, L., Kennicutt, R. C., Jr., & Saha, A. 2004, ApJ, 608, 42
Sand, D. J., Treu, T., Ellis, R. S., & Smith, G. P. 2005, ApJ, 627, 32
Sharon, K., Gladders, M. D., Rigby, J. R., et al. 2012, ApJ, 746, 161
Smith, G. P., Kneib, J.-P., Smail, I., et al. 2005, MNRAS, 359, 417
Soucail, G., Mellier, Y., Fort, B., Mathez, G., & Hammer, F. 1987, A&A, 184, L7
Storchi-Bergmann, T., Calzetti, D., & Kinney, A. L. 2004, ApJ, 429, 572
Storchi-Bergmann, T., Kinney, A. L., & Challis, P. 2005, ApJS, 98, 103
Taylor, V. A., Jansen, R. A., Windhorst, R. A., et al. 2005, ApJ, 630, 784
Vacca, W. D., & Conti, P. S. 1992, ApJ, 401, 543
Weißmann, A., Böhringer, H., Šuhada, R., & Ameglio, S. 2013, A&A, 549, A19
Welikala, N., & Kneib, J.-P. 2012, ApJ, submitted (arXiv:1202.0494)
Yuan, T.-T., Kewley, L. J., Swinbank, A. M., & Richard, J. 2012, ApJ, 759, 66
Yuan, T.-T., Kewley, L. J., Swinbank, A. M., Richard, J., & Livermore, R. C. 2011, ApJL, 732, L14
Zheng, W., Bradley, L. D., Bouwens, R. J., et al. 2009, ApJ, 697, 1907
Zwicky, F. 1937, PhRv, 51, 290